Advanced Quantum Technologies

ADVANCED QUANTUM TECHNOLOGIES
www.advquantumtech.com

RESEARCH ARTICLE OPEN ACCESS

Violation of Qudit Mermin's Inequality and Its Application to Quantum Computing

Jinwon Yoo[1] | Stefania Sciara[1,2] | Nicola Montaut[1] | Agnes George[1] | Roberto Morandotti[1]

[1]Institut national de la recherche scientifique – Centre Énergie Matériaux et Télécommunications (INRS-EMT), Varennes, Québec, Canada | [2]Département de génie électrique, École de technologie supérieure (ÉTS), Montréal, QC, Canada

Correspondence: Stefania Sciara (stefania.sciara@etsmtl.ca) | Roberto Morandotti (roberto.morandotti@inrs.ca)

Received: 4 November 2025 | **Revised:** 10 February 2026 | **Accepted:** 2 March 2026

Keywords: High-dimensional measurement-based quantum computation| High-dimensional multipartite nonlocality| Qudit Greenberger–Horne–Zeilinger (GHZ) states

ABSTRACT

Mermin's inequality provides a fundamental test to verify the quantum nonlocality of multipartite Greenberger–Horne–Zeilinger (GHZ) states, by also serving as a key resource for measurement-based quantum computing. While the theoretical foundation of Mermin's inequality test is well established for both qubit and qudit systems, the experimental validation for qudits remains elusive. In this work, we perform qudit Mermin's inequality test implemented on a qutrit (i.e., three-level system) GHZ state, where the multipartition is achieved by deterministically entangling the time and frequency bins of a biphoton state via standard fiber-optic components. The direct measurement of Mermin's operator yields an expectation value of 8.612(44), surpassing the bound of 6 for local realism by 59 standard deviations. We demonstrate the potential of the verified GHZ state for high-dimensional quantum computing by utilizing the nonlocality results to compute a ternary logic function through non-adaptive high-dimensional measurement-based quantum computation. Our scheme is readily scalable to higher dimensions without additional loss or modifications to the experimental setup.

1 | Introduction

Formulated in 1990 [1], Mermin's inequality extends the concept of Bell's theorem to multi-partite systems, offering fundamental and experimental methods to validate the violation of local realism beyond two-partite Bell states. Initially designed for qubit spins, this inequality is evaluated by measuring the expectation value of Mermin's operator, which consists of a specific set of 2×2 unitary operators—namely, Pauli matrices [1]. Initial demonstrations of nonlocality in multi-partite systems have shown that Mermin's inequality is only violated by Greenberger-Horne-Zeilinger (GHZ) states [2]. The nonlocal properties of GHZ states have been experimentally validated across a wide range of qubit platforms, including photonics [3–7], ion traps [8], and superconductors [9, 10]. Crucially, this nonlocality serves as a valuable resource for measurement-based quantum computation, where GHZ correlations are harnessed to implement gate operations through local (single-partite) measurements [11, 12].

Recently, Mermin's inequality has been theoretically extended to multipartite qudit (i.e., d-level system with $d \geq 3$) GHZ states, where a key distinction lies in the use of $d \times d$ unitary operators [13–18]. Beyond their foundational interest, d-level correlations provide a foundation for high-dimensional measurement-based quantum computation, enabling greater information density per system and reduced overhead compared with qubit-based schemes [18, 19]. Realizing both the inequality test and high-dimensional computation requires simultaneous d-level projections across multiple parties, which introduces challenges such as maintaining coherence and minimizing crosstalk between levels. For instance, Mermin's inequality test for a qutrit (i.e., three-level system) GHZ state has been recently performed using three

photons entangled in the orbital angular momentum degree of freedom (DoF) [20]. However, due to the limitations associated with probabilistic state preparation and the complexity of high-dimensional projections in multiphoton systems, the expectation value of Mermin's operator was inferred by measuring quantum state fidelity via two-level projections only. A direct experimental demonstration of quantum nonlocality in multipartite qutrit GHZ states via high-dimensional projections has been achieved only very recently using a path identity scheme [21]. Yet, the computational framework enabled by d-level correlations has remained largely unexplored.

Bridging this gap between high-dimensional correlation and computation, we present the experimental violation of qudit Mermin's inequality using a three-qutrit GHZ state, together with a demonstration of its computational power. Our approach to multipartite qudit preparation involves the use of a deterministic high-dimensional entangling gate—the SUM gate—between the time and frequency DoFs of a biphoton frequency comb. This method allows us to efficiently perform three-level projection measurements using standard fiber-optic infrastructure, leading to a direct experimental violation of Mermin's inequality by 59 standard deviations. We showcase the potential of the verified GHZ state for advanced computational architectures through non-adaptive high-dimensional measurement-based quantum computation [18].

2 | Results

2.1 | High-Dimensional Multi-Partite Nonlocality

The three-qutrit GHZ state serves as a fundamental resource for demonstrating high-dimensional multi-partite nonlocality, defined as

$$|\,\mathrm{GHZ}\rangle = \frac{1}{\sqrt{3}}(|\,000\rangle + |\,111\rangle + |\,222\rangle) \tag{1}$$

The nonlocality of the three-qutrit GHZ state can be tested by applying Mermin's operator on the GHZ state, given by [16]:

$$\begin{aligned} M = XXX + q^2\,(YYY + XYW + XWY + YXW + WXY \\ + YWX + WYX) + qWWW \end{aligned} \tag{2}$$

where $q = e^{2\pi i/3}, X = \sum_{s=0}^{2} |s+1(\mathrm{mod}\ 3)\rangle\langle s|, Y = Z^{1/3}XZ^{-1/3}$, $W = Z^{2/3}XZ^{-2/3}$, and $Z = \sum_{k=0}^{2} |k\rangle q^k \langle k|$. The nine elements in Equation (2) are non-Hermitian and share the GHZ state in Equation (1) as a common eigenstate, with complex eigenvalues of unit magnitude. The coefficients of the elements in Mermin's operator align the complex phases (i.e., the arguments) of their eigenvalues so that they combine constructively, yielding the maximal quantum expectation value, $|\langle M_Q\rangle| = 9$. Here $\langle\cdot\rangle$ denotes the expectation value and $|\cdot|$ its absolute value. In contrast, within the framework of local hidden variable (LHV) theories, which assume pre-existing local properties of each party, the expectation value of Mermin's operator is bounded by $|\langle M_{\mathrm{LHV}}\rangle| \leq 6$, because classical assignments cannot satisfy all nine correlations simultaneously [16].

2.2 | Non-Adaptive High-Dimensional Measurement-Based Quantum Computation

The nonlocality proven by Mermin's inequality test is directly linked to the ability of performing non-adaptive high-dimensional measurement-based quantum computation (NHMQC) through qudit GHZ states [18, 22, 23]. The computational framework of NHMQC evaluates a multivariate modular arithmetic function of the form $f : \{0,1,\ldots,d-1\}^p \to \{0,1,\ldots,d-1\}$, where p represents the number of input variables and d denotes the dimensionality of the inputs. Unlike the adaptive approach, which requires random measurements with feedforward control [24–26], NHMQC employs pre-determined measurement settings, thereby providing a straightforward platform to probe the fundamental resources underpinning high-dimensional measurement-based quantum computation [11, 12, 18].

For the ternary case based on qutrit GHZ states, fixed local measurements enable the evaluation of modular polynomial functions of algebraic degree beyond two, whereas any LHV model is fundamentally restricted to functions of degree at most two [18]. This enhanced computational capability originates from the genuine multipartite nonlocal correlations of the GHZ state [18]. Consequently, NHMQC not only provides an operational model of high-dimensional quantum computation, but also serves as a witness of nonlocal correlations beyond classical hidden-variable theories, as tested through the qutrit Mermin's inequality in this work.

2.3 | Three-Qutrit GHZ State: Generation Scheme and Experimental Setup

To generate a three-qutrit GHZ state, we initially create frequency- and time-correlated photon pairs through spontaneous nonlinear process (Figure 1a). A comb-like spectral filter is then applied to both photons, selecting three discrete frequency-correlated pairs (Figure 1b), which results in a biphoton frequency comb state $|\psi_0\rangle = |t_0\rangle_s\,|t_0'\rangle_i \frac{1}{\sqrt{3}} \sum_{j=0}^{2} |f_j\rangle_s |f_j'\rangle_i$. Here, f and f' are the central frequencies of the signal (s) and idler (i) photons, j is the index of the frequency-correlated pairs, while $|t_0\rangle_s$ and $|t_0'\rangle_i$ are the initial time-bin states. A high-dimensional entangling SUM gate is applied to the idler photon through a dispersive medium which linearly time-shifts its frequency bins (Figure 1c) [27]. This operation entangles the frequency $|f_0'\rangle_i$, $|f_1'\rangle_i$, $|f_2'\rangle_i$ and the corresponding time $|t_0'\rangle_i$, $|t_1'\rangle_i$, $|t_2'\rangle_i$ bins of the idler, while leaving the signal photon state unchanged [28]. The resulting quantum state can be expressed as

$$\begin{aligned} |\psi_1\rangle = \frac{1}{\sqrt{3}} \Big(|f_0\rangle_s |f_0'\rangle_i |t_0'\rangle_i \\ + |f_1\rangle_s |f_1'\rangle_i |t_1'\rangle_i + |f_2\rangle_s |f_2'\rangle_i |t_2'\rangle_i \Big) |t_0\rangle_s \end{aligned} \tag{3}$$

By defining the encoding $|f_0/f_0'/t_0'\rangle \equiv |0\rangle$, $|f_1/f_1'/t_1'\rangle \equiv |1\rangle$, $|f_2/f_2'/t_2'\rangle \equiv |2\rangle$, and neglecting the time-bin state $|t_0\rangle_s$ of the signal photon, the state $|\psi_1\rangle$ can be described as a three-qutrit GHZ state, as given in Equation (1).

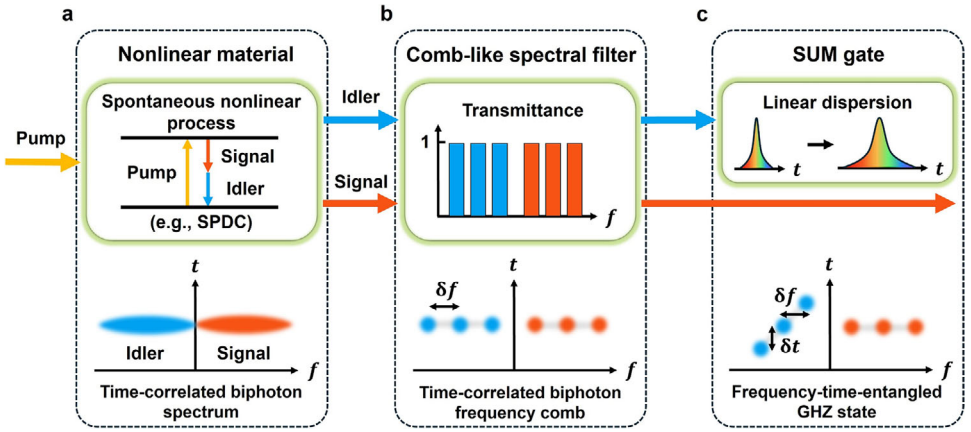

FIGURE 1 | Time-frequency-entangled three-qutrit GHZ state generation scheme. a) A spontaneous nonlinear process, such as spontaneous parametric down conversion (SPDC), generates time-correlated photon pairs (signal and idler) within a nonlinear material. b) The spectrum of these photon pairs is shaped using a comb-like spectral filter, producing a time-correlated biphoton frequency comb (here, three frequency-correlated pairs are selected). c) A SUM gate is applied to one of the photon pair (here, the idler) to entangle time and frequency. This is achieved by sending the idler photon to a linearly dispersive medium, where frequency bins of the idler photon are time-shifted, resulting in a frequency-time-entangled three-qutrit GHZ state.

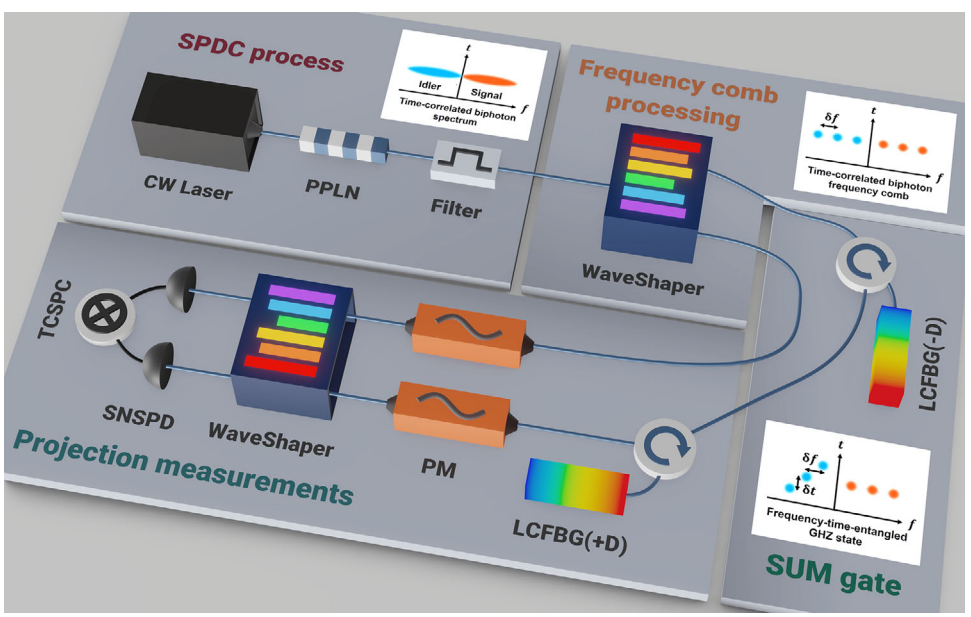

FIGURE 2 | Experimental setup. A single-photon pair is generated via the spontaneous parametric down-conversion (SPDC) process by pumping a periodically poled lithium niobate (PPLN) crystal with a continuous wave (CW) laser. A time-correlated biphoton frequency comb is produced through spectral filtering using a WaveShaper. The frequency-time-entangled GHZ state is created by applying a SUM gate to the idler photon using a negatively dispersed linearly chirped fiber Bragg grating (LCFBG). Projection measurements for state characterization, Mermin's inequality test, interference measurement and non-adaptive high-dimensional measurement-based quantum computation are carried out using a positively dispersed LCFBG for the time qudit in the idler photon, and a phase modulator (PM) for the frequency qudits in both the signal and idler photons. The projected photons undergo further spectral filtering with another WaveShaper before being detected by superconducting nanowire single-photon detectors (SNSPDs) connected to a time-correlated single photon counting (TCSPC) unit. Blue and black lines represent polarization-maintaining fibers and SMA cables, respectively.

Figure 2 illustrates the experimental setup. A periodically poled lithium niobate (PPLN) waveguide is pumped using a continuous-wave (CW) laser at the central frequency of 775.5 nm to generate signal-idler photon pairs through SPDC. A 1550 nm bandpass filter is used to isolate the photon pairs. The photons pass through a WaveShaper, which filters out three equidistant frequency-correlated pairs to create a biphoton frequency comb [28, 29]. A SUM gate is applied to the idler photons by sending them through a negatively dispersed (−D) linearly chirped fiber Bragg grating (LCFBG). This induces a deterministic time shift to the frequency bins of the idler corresponding to the amount of dispersion applied. Therefore, the processed idler state, together

with the signal photon, generates a time-frequency entangled two-photon state, corresponding to the three-qutrit GHZ state. The detailed procedure for generating the three-qutrit GHZ state is provided in the Experimental Section/Methods.

The generated GHZ state is characterized via projection measurements on each qutrit in both the frequency and time domains. Frequency-bin measurements are accomplished through a frequency-mixing technique, facilitated by a phase modulator in the path of each photon [30]. Time-bin measurements on the idler photon are achieved by employing an equally, but positively dispersed (+D) LCFBG (see Figure 2), which deterministically projects all time bins into a specific temporal mode. Another WaveShaper is then used in the measurement stage to filter out the mixed frequencies on the signal and idler photons, which are routed thereafter to two superconducting nanowire single-photon detectors (SNSPDs) (Section S1).

2.4 | Experimental Verification of Three-Qutrit GHZ State

To verify the GHZ state generation, we estimate fidelity through the expression [31]:

$$F_{\mathrm{GHZ}} = \frac{1}{3}\sum_{n=0}^{2}\langle nnn\,|\rho|\,nnn\rangle + \frac{1}{3}\sum_{\substack{n,m=0\\ n\neq m}}^{2} Re\,\langle nnn\,|\rho|\,mmm\rangle \tag{4}$$

where ρ denotes the measured density matrix of the GHZ state, and n and m are subspaces representing the basis states $|0\rangle$, $|1\rangle$, and $|2\rangle$ of each qutrit. The fidelity has a lower bound of 2/3, and values exceeding this threshold are required to validate the demonstration of a three-qutrit GHZ state [20, 31]. Figure 3 shows the measured values used for estimating the elements in Equation (4) (see Experimental Section/Methods). The calculated fidelity is $F = 0.958(10)$, significantly surpassing the lower bound of 2/3 by 29 standard deviations and establishing the realization of a three-qutrit GHZ state. To exclude all biseparable models and further certify genuine multipartite entanglement, we evaluate an entanglement witness, yielding $\langle \mathcal{W}_{\mathrm{GHZ}}\rangle = -0.937(15)$, whose negative expectation value unambiguously indicates entanglement beyond the biseparable bound (Section S2).

2.5 | Experimental Test of Qutrit Mermin's Inequality

Using the verified three-qutrit GHZ state, we perform the qutrit Mermin's inequality test by measuring the expectation values of the nine elements in Equation (2), obtained by projecting the GHZ state onto their corresponding eigenvectors (Section S3). By summing the expectation values of all elements, presented in Figure 4, we obtain the expectation value of the qutrit Mermin's operator, $|\langle M_{\mathrm{meas}}\rangle| = 8.612(44)$, which is in close agreement with the quantum mechanical prediction of 9. This result demonstrates a significant violation of the LHV value of 6 by 59 standard deviations, strongly confirming the quantum mechanical prediction and ruling out classical explanations of the observed correlations.

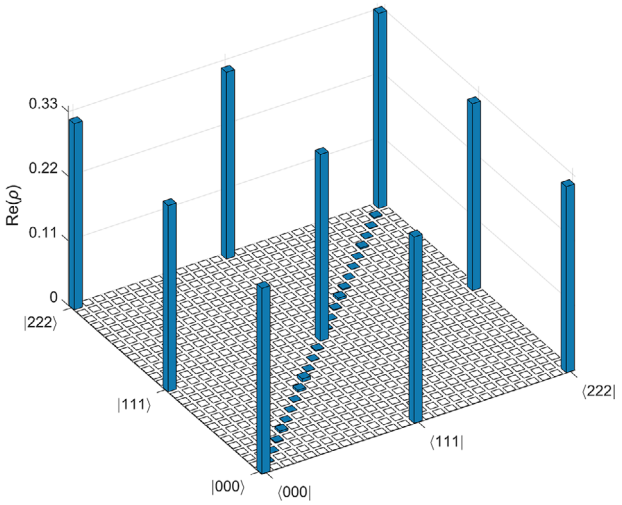

FIGURE 3 | Density matrix elements used for the fidelity calculation of the GHZ state. The elements included in the fidelity calculation are marked in blue, while those not utilized are denoted in white. The measured fidelity is $F = 0.958(10)$, where the number in parentheses denotes the uncertainty in the last digits (i.e., $F = 0.958 \pm 0.010$). This value exceeds the verification bound of 2/3 by 29 standard deviations, confirming the presence of a three-qutrit GHZ state.

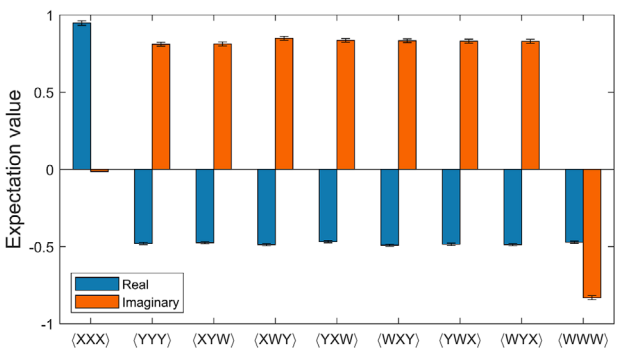

FIGURE 4 | Expectation values of nine elements of the qutrit Mermin's operator. Note that the expectation values are complex, given the non-Hermitian nature of the observables. The expectation value of Mermin's operator is $|\langle M_{\mathrm{meas}}\rangle| = 8.612(44)$, surpassing the LHV bound of 6 by 59 standard deviations. Error bars are determined by Poissonian statistics.

We further assess the violation of qutrit Mermin's inequality by examining the visibility of quantum interference. We first set a lower bound for visibility, determined from the LHV theorems, which is established at 0.75 (Section S4). We then measure the visibility from the quantum interference pattern. To this end, each qutrit of the GHZ state is projected onto the state $|\phi\rangle = \frac{1}{\sqrt{3}}(|0\rangle + e^{i\theta}|1\rangle + e^{i2\theta}|2\rangle)$, with the phase θ being systematically varied from 0 to 2π (Section S4). Figure 5 shows the measured quantum interference pattern, which exhibits excellent agreement with the theoretical one. We extract a raw visibility of $V = 0.992(7)$, exceeding the LHV bound of 0.75 by 34 standard deviations. This outcome conclusively confirms the violation of the qutrit Mermin's inequality (Section S4).

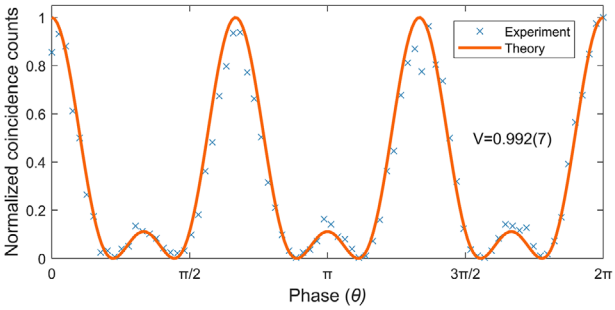

FIGURE 5 | Interference measurement for Mermin's inequality test. The raw visibility is $V = 0.992(7)$, significantly exceeding the local realism upper bound of 0.75 by 34 standard deviations, thereby confirming the violation of Mermin's inequality. The cross marks represent the experimental data, while the solid line depicts the theoretically estimated interference pattern.

2.6 | Demonstration of High-Dimensional Quantum Computation

In our demonstration, we compute a ternary logic third-degree polynomial function [18]:

$$f\ (x) = x_0^2\ \oplus x_1^2 \oplus x_0 x_1 \oplus 2\left[x_0^2 x_1 \oplus x_1^2 x_0\right] \tag{5}$$

We transform the two input variables x_0 and x_1 into three elements by pre-processing: $s_0 = x_0$, $s_1 = x_1$, and $s_2 = 2(x_0 \oplus x_1)$. Each qutrit of the GHZ state is then measured using the corresponding operators $\hat{m}_0(s_0)$, $\hat{m}_1(s_1)$, and $\hat{m}_2(s_2)$. Further details of the experimental procedure are provided in Section S5. Table 1 provides the computational results for all possible input combinations. The experimental outcomes are highly consistent with the theoretical predictions, showing an average relative error of 0.329% only. The success probability of our computation, derived from the result of qutrit Mermin's inequality test (Section S6), is 0.971, underscoring the efficacy of our GHZ state in executing high-dimensional quantum computation. Furthermore, this success probability surpasses the 0.778 bound predicted by LHV theorems (Section S6), additionally highlighting the nonlocal characteristics inherent to our GHZ state.

3 | Conclusion

We have experimentally validated the multipartite qudit nonlocality on a three-partite qutrit GHZ state, by directly assessing the expectation value of the qutrit Mermin's operator via three-level projections across all parties simultaneously. We found that such a value significantly exceeded the threshold predicted by the LHV theory. The deterministically generated qutrit GHZ state showed a quantum state fidelity of 0.958(10), much higher than the values of ≈0.73–0.91 achieved in probabilistic multi-photon experiments [20, 21, 32].

As a fair note, we acknowledge that our Mermin's inequality test is not free of loopholes such as spatial locality, as the hyper-encoding approach inherently hinders us from spatially separating the two parties (i.e., the time and frequency bins) within a single photon. As an alternative, one could explore pumping a photon-triplet source with a pulsed laser to directly generate a time-bin three-qudit GHZ state [33, 34], which could help overcome these limitations. However, a loophole-free nonlocality test falls outside the scope of this work. Instead, we focused on demonstrating how nonlocality can be experimentally applied to high-dimensional quantum computation. By leveraging the high-dimensional nature and nonlocality of the demonstrated qutrit GHZ state, we have successfully computed a ternary logic third-degree polynomial function with minimal error, marking the first implementation of high-dimensional measurement-based quantum computation. The success rate close to one highlights the fundamental role of d-level correlations in this type of operation. While previous experiments utilized multipartite qudit cluster states for high-dimensional one-way quantum processing [35], our work is intrinsically different, as it demonstrates the implementation of a specific measurement-based computational problem.

The proposed scheme for qudit GHZ state offers the advantage of being easily scaled up to higher dimensions by, e.g., incorporating additional frequency-bin pairs, without introducing additional losses and/or modifying the experimental setup. Combining the scalability stemming from few-photon state implementations with the use of off-the-shelf fiber-optic technology will sup-

TABLE 1 | Computational results of the NHMQC using three-qutrit GHZ state.

x_0	x_1	$\langle \hat{m}_0(s_0)\hat{m}_1(s_1)\hat{m}_2(s_2)\rangle$	Output z	Exact value $f(x_0, x_1)$	Relative error (%)
0	0	$0.948e^{i(-0.015)}$	2.993	0 (≡ 3 mod 3)	0.243
0	1	$0.941e^{i(2.100)}$	1.003	1	0.259
0	2	$0.979e^{i(2.092)}$	0.999	1	0.095
1	0	$0.957e^{i(2.081)}$	0.994	1	0.628
1	1	$0.942e^{i(2.105)}$	1.005	1	0.527
1	2	$0.962e^{i(2.099)}$	1.002	1	0.237
2	0	$0.967e^{i(2.103)}$	1.004	1	0.420
2	1	$0.962e^{i(2.102)}$	1.004	1	0.383
2	2	$0.955e^{i(4.196)}$	2.004	2	0.174

Here, $s_0 = x_0$, $s_1 = x_1$, and $s_2 = 2(x_0 \oplus x_1)$. The relative error represents the ratio of the absolute difference between the exact value and the experimental result to the exact value, expressed as a percentage. The average relative error is 0.329%.

port the development of advanced, yet easily implementable, photonic-based quantum computing architectures [36, 37].

4 | Experimental Section/Methods

4.1 | Qutrit GHZ State Generation

A periodically poled lithium niobate (PPLN) waveguide is pumped using a continuous wave (CW) laser (QPhotonics, QFBGLD-775-5) at the central frequency of 775.5 nm (386.58 THz) to generate broadband energy-time correlated single photon pairs (signal and idler). A 1550 nm (193.414 THz) bandpass filter (OZ Optics) with a 78 nm transmission bandwidth (1500–1578 nm) is used to isolate the photon pairs. To generate a time-correlated biphoton frequency comb of two frequency-bin qutrits, we use a WaveShaper (Finisar, 4000S) to filter out three equidistant frequency-correlated pairs (1535.735, 1536.003, 1536.271 nm for signal photon and 1565.921, 1566.199, 1566.477 nm for idler photon, with each frequency's bandwidth of $\Delta f = 27$ GHz). The WaveShaper separates the signal and idler photons, sending the idler to the negative linearly chirped fiber Bragg grating (LCFBG) with a dispersion of around -2 ns nm^{-1}. The negative LCFBG induces a linear time shift in the idler photon's frequency bins, implementing a SUM gate (see Experimental Section/Methods). The spacing between time bins is approximately $\delta t = 570$ ps, with each bin's width of around $\Delta t = 288$ ps. The characteristics of our frequency and time qutrits exceed the Fourier uncertainty limit, with $\delta f \delta t = 19.38 > 1$, enabling their independent control and measurement in a hyper-encoding approach [35]. Therefore, the processed idler state, together with the signal photon, generates a time-frequency entangled two-photon state, corresponding to the three-qutrit GHZ state.

4.2 | SUM Gate

The SUM gate is a generalized version of controlled-NOT gate that entangles two qudits, each stored in two registers: the control (c) and target (t) registers. This gate is defined as [27]:

$$\mathrm{SUM}_d = \sum_{k=0}^{d-1} |k\rangle\langle k| \otimes {X_d}^k \tag{6}$$

where the d-level Pauli-X gate, $X_d = \sum_{x=0}^{d-1} |x+1 \pmod d\rangle\langle x|$, is applied to the target register qudit k times, conditioned by the control register qudit state $|k\rangle$ ($k \neq \mathbb{Z}_d$). This gate enables the entangling of the two qudits based on the specific control and target register. When the SUM_3 is applied to the state $\frac{1}{\sqrt{3}}(|0\rangle_c + |1\rangle_c + |2\rangle_c)|0\rangle_t$, the target register qudit state is shifted, and the output state becomes entangled in a Bell-like state $\frac{1}{\sqrt{3}}(|0\rangle_c|0\rangle_t + |1\rangle_c|1\rangle_t + |2\rangle_c|2\rangle_t)$. In our experiment, the frequency degree of freedom of the idler photon acted as control qudit, while its time degree of freedom acted as target qudit. A negative LCFBG was used to apply dispersion-shift of the frequency-bin state into the time-bin domain.

4.3 | Fidelity Measurement

To determine the fidelity of our three-qutrit GHZ state, we need to measure the three diagonal elements of its density matrix, that is $\langle 000|\rho|000\rangle$, $\langle 111|\rho|111\rangle$, and $\langle 222|\rho|222\rangle$, along with its six anti-diagonal elements, $\langle 000|\rho|111\rangle$, $\langle 111|\rho|000\rangle$, $\langle 000|\rho|222\rangle$, $\langle 222|\rho|000\rangle$, $\langle 222|\rho|111\rangle$, and $\langle 111|\rho|222\rangle$. For the diagonal elements, we direct the signal and idler photons to the SNSPDs and measure the basis states of each qutrit. The anti-diagonal elements are measured using specific combinations of the 2×2 Pauli matrices σ_x and σ_y [31]. The real and imaginary parts of each component are given by:

$$\begin{aligned} &Re\left(\langle nnn|\,\rho\,|mmm\rangle\right) \\ &= \frac{1}{8}\left(\left\langle \sigma_x^{(n,m)}\sigma_x^{(n,m)}\sigma_x^{(n,m)}\right\rangle - \left\langle \sigma_x^{(n,m)}\sigma_y^{(n,m)}\sigma_y^{(n,m)}\right\rangle\right. \\ &\left. - \left\langle \sigma_y^{(n,m)}\sigma_x^{(n,m)}\sigma_y^{(n,m)}\right\rangle - \left\langle \sigma_y^{(n,m)}\sigma_y^{(n,m)}\sigma_x^{(n,m)}\right\rangle\right) \end{aligned} \tag{7}$$

$$\begin{aligned} &Im\left(\langle nnn|\,\rho\,|mmm\rangle\right) \\ &= \frac{1}{8}\left(\left\langle \sigma_y^{(n,m)}\sigma_y^{(n,m)}\sigma_y^{(n,m)}\right\rangle - \left\langle \sigma_y^{(n,m)}\sigma_x^{(n,m)}\sigma_x^{(n,m)}\right\rangle\right. \\ &\left. - \left\langle \sigma_x^{(n,m)}\sigma_y^{(n,m)}\sigma_x^{(n,m)}\right\rangle - \left\langle \sigma_x^{(n,m)}\sigma_x^{(n,m)}\sigma_y^{(n,m)}\right\rangle\right) \end{aligned} \tag{8}$$

where $\sigma_x^{(n,m)} = |m\rangle\langle n| + |n\rangle\langle m|$ and $\sigma_y^{(n,m)} = i|m\rangle\langle n| - i|n\rangle\langle m|$, in the subspaces n, m. We measure the expectation value of the operators $\sigma_x^{(n,m)}$ and $\sigma_y^{(n,m)}$ by projecting the GHZ state into their superposed eigenvectors. Further details of the experimental procedure are provided in Section S1.

Acknowledgements

J.Y. would like to thank Kwangil Bae for discussion on Mermin's inequality test. We acknowledge QuantumOpus and Nick Bertone from OptoElectronics Components for their help and for providing us with state-of-the-art superconducting nanowire single-photon detection equipment.

Funding

S.S. and N.M. acknowledge the financial support from Mitacs Elevate Thematic Quantum Science. R.M. acknowledges support from the Canada Research Chairs program, as well as from NSERC, through the following projects: AQUA ALLRP 587602–23, QuEnSi ALLRP 578468-22, Consortium on Integrated Quantum Photonics with Ferroelectric Materials ALLRP 587352-23, HyperSpace ALLRP 569583-21, and from FRQNT, through the project AdéQuATS FRQNT 328872.

Conflicts of Interest

The authors declare no conflicts of interest.

Data Availability Statement

The data that support the findings of this study are available from the corresponding authors upon request.

References

1. N. D. Mermin, "Extreme Quantum Entanglement in a Superposition of Macroscopically Distinct States," *Physical Review Letters* 65, no. 15 (1990): 1838–1840.

2. D. M. Greenberger, M. A. Horne, A. Shimony, and A. Zeilinger, "Bell's Theorem without Inequalities," *American Journal of Physics* 58, no. 12 (1990): 1131–1143.

3. J.-W. Pan, D. Bouwmeester, M. Daniell, H. Weinfurter, and A. Zeilinger, "Experimental Test of Quantum Nonlocality in Three-Photon Greenberger–Horne–Zeilinger Entanglement," *Nature* 403, no. 6769 (2000): 515–519.

4. Z. Zhao, T. Yang, Y.-A. Chen, A.-N. Zhang, M. Żukowski, and J.-W. Pan, "Experimental Violation of Local Realism by Four-Photon Greenberger-Horne-Zeilinger Entanglement," *Physical Review Letters* 91, no. 18 (2003): 180401.

5. C. Erven, E. Meyer-Scott, K. Fisher, et al., "Experimental Three-Photon Quantum Nonlocality under Strict Locality Conditions," *Nature Photonics* 8, no. 4 (2014): 292–296.

6. J. Zhao, M. Wang, B. Sun, et al., "Preparation and Analysis of Two-Dimensional Four-Qubit Entangled States with Photon Polarization and Spatial Path," *Entropy* 24, no. 10 (2022): 1388.

7. H.-X. Lu, L.-Z. Cao, J.-Q. Zhao, Y.-D. Li, and X.-Q. Wang, "Extreme Violation of Local Realism with a Hyper-Entangled Four-Photon-Eight-Qubit Greenberger-Horne-Zelinger State," *Scientific Reports* 4, no. 1 (2014): 4476.

8. B. P. Lanyon, M. Zwerger, P. Jurcevic, et al., "Experimental Violation of Multipartite Bell Inequalities with Trapped Ions," *Physical Review Letters* 112, no. 10 (2014): 100403.

9. M. Neeley, R. C. Bialczak, M. Lenander, et al., "Generation of Three-Qubit Entangled States Using Superconducting Phase Qubits," *Nature* 467, no. 7315 (2010): 570–573.

10. L. DiCarlo, M. D. Reed, L. Sun, et al., "Preparation and Measurement of Three-Qubit Entanglement in a Superconducting Circuit," *Nature* 467, no. 7315 (2010): 574–578.

11. J. Anders and D. E. Browne, "Computational Power of Correlations," *Physical Review Letters* 102, no. 5 (2009): 050502.

12. M. Frembs, S. Roberts, E. T. Campbell, and S. D. Bartlett, "Hierarchies of Resources for Measurement-Based Quantum Computation," *New Journal of Physics* 25, no. 1 (2023): 013002.

13. J. Lawrence, "Rotational Covariance and Greenberger-Horne-Zeilinger Theorems for Three or More Particles of any Dimension," *Physical Review A* 89, no. 1 (2014): 012105.

14. J. Ryu, C. Lee, M. Żukowski, and J. Lee, "Greenberger-Horne-Zeilinger Theorem for N Qudits," *Physical Review A* 88, no. 4 (2013): 042101.

15. J. Ryu, C. Lee, Z. Yin, et al., "Multisetting Greenberger-Horne-Zeilinger Theorem," *Physical Review A* 89, no. 2 (2014): 024103.

16. J. Lawrence, "Mermin Inequalities for Perfect Correlations in Many-Qutrit Systems," *Physical Review A* 95, no. 4 (2017): 042123.

17. W. Tang, S. Yu, and C. Oh, "Multisetting Greenberger-Horne-Zeilinger Paradoxes," *Physical Review A* 95, no. 1 (2017): 012131.

18. J. Mackeprang, D. Bhatti, M. Hoban, and S. Barz, "The Power of Qutrits for Non-Adaptive Measurement-Based Quantum Computing," *New Journal of Physics* 25, no. 7 (2023): 073007.

19. S. Paesani, J. F. Bulmer, A. E. Jones, R. Santagati, and A. Laing, "Scheme for Universal High-Dimensional Quantum Computation with Linear Optics," *Physical Review Letters* 126, no. 23 (2021): 230504.

20. M. Erhard, M. Malik, M. Krenn, and A. Zeilinger, "Experimental Greenberger–Horne–Zeilinger Entanglement beyond Qubits," *Nature Photonics* 12, no. 12 (2018): 759–764.

21. X.-M. Hu, C.-X. Huang, N. d'Alessandro, et al., "Observation of Genuine High-Dimensional Multi-Partite Non-Locality in Entangled Photon States," *Nature Communications* 16, no. 1 (2025): 5017.

22. B. Demirel, W. Weng, C. Thalacker, M. Hoban, and S. Barz, "Correlations for Computation and Computation for Correlations," *npj Quantum Information* 7, no. 1 (2021): 29.

23. J. Mackeprang, D. Bhatti, and S. Barz, "Non-Adaptive Measurement-Based Quantum Computation on Ibm Q," *Scientific Reports* 13, no. 1 (2023): 15428.

24. P. Walther, K. J. Resch, T. Rudolph, et al., "Experimental One-Way Quantum Computing," *Nature* 434, no. 7030 (2005): 169–176.

25. R. Prevedel, P. Walther, F. Tiefenbacher, et al., "High-Speed Linear Optics Quantum Computing Using Active Feed-Forward," *Nature* 445, no. 7123 (2007): 65–69.

26. O. Lib and Y. Bromberg, "Resource-Efficient Photonic Quantum Computation with High-Dimensional Cluster States," *Nature Photonics* 18, no. 11 (2024): 1218–1224.

27. J. Daboul, X. Wang, and B. C. Sanders, "Quantum Gates on Hybrid Qudits," *Journal of Physics A: Mathematical and General* 36, no. 10 (2003): 2525–2536.

28. P. Imany, J. A. Jaramillo-Villegas, M. S. Alshaykh, et al., "High-Dimensional Optical Quantum Logic in Large Operational Spaces," *npj Quantum Information* 5, no. 1 (2019): 59.

29. P. Imany, O. D. Odele, J. A. Jaramillo-Villegas, D. E. Leaird, and A. M. Weiner, "Characterization of Coherent Quantum Frequency Combs Using Electro-Optic Phase Modulation," *Physical Review A* 97, no. 1 (2018): 013813.

30. M. Kues, C. Reimer, P. Roztocki, et al., "On-Chip Generation of High-Dimensional Entangled Quantum States and Their Coherent Control," *Nature* 546, no. 7660 (2017): 622–626.

31. A. Cervera-Lierta, M. Krenn, A. Aspuru-Guzik, and A. Galda, "Experimental High-Dimensional Greenberger-Horne-Zeilinger Entanglement with Superconducting Transmon Qutrits," *Physical Review Applied* 17, no. 2 (2022): 024062.

32. J. Bao, Z. Fu, T. Pramanik, et al., "Very-Large-Scale Integrated Quantum Graph Photonics," *Nature Photonics* 17, no. 7 (2023): 573–581.

33. D. R. Hamel, L. K. Shalm, H. Hübel, et al., "Direct Generation of Three-Photon Polarization Entanglement," *Nature Photonics* 8, no. 10 (2014): 801–807.

34. H. Yu, S. Sciara, M. Chemnitz, et al., "Quantum Key Distribution Implemented with D-Level Time-Bin Entangled Photons," *Nature Communications* 16, no. 1 (2025): 171.

35. C. Reimer, S. Sciara, P. Roztocki, et al., "High-Dimensional One-Way Quantum Processing Implemented on D-Level Cluster States," *Nature Physics* 15, no. 2 (2019): 148–153.

36. M. Frembs, S. Roberts, and S. D. Bartlett, "Contextuality as a Resource for Measurement-Based Quantum Computation beyond Qubits," *New Journal of Physics* 20, no. 10 (2018): 103011.

37. M. J. Hoban, J. J. Wallman, and D. E. Browne, "Generalized Bell-Inequality Experiments and Computation," *Physical Review A* 84, no. 6 (2011): 062107.

Supporting Information

Additional supporting information can be found online in the Supporting Information section.

Supporting File: qute70255-sup-0001-SuppMat.docx.